Carbon fibre with and without a protective ultrathin alumina film grafted with carbon nanotubes for hierarchical composites observed by ptychographic X-ray computed tomography

W. Szmyt*[1,2,3], S. Vogel[1,2,3], M. Holler[2], A. Diaz[2], J. Gobrecht[2], M. Calame[3,4] and C. Dransfeld[1]

[1]Institute of Polymer Engineering, FHNW University of Applied Sciences and Arts Northwestern Switzerland, 5210 Windisch, Switzerland, Web Page: http://www.fhnw.ch
[2] Paul Scherrer Institut, 5232 Villigen, Switzerland, Web Page: https://www.psi.ch
[3] Department of Physics, University of Basel, 4056 Basel, Switzerland, Web Page: https://physik.unibas.ch/
[4] Swiss Nanoscience Institute, University of Basel, 4056 Basel, Switzerland, Web Page: https://www.nanoscience.ch/
*Email: Wojciech.Szmyt@fhnw.ch

Keywords: hierarchical composites, carbon fibre, carbon nanotubes, PXCT, iron nanoparticles

Abstract
The failure of carbon fibre reinforced polymers (CFRP) is typically governed by compressive failure in the fibre direction or insufficient transverse strength and occurs at a fibre-matrix interface. A novel approach of enhancement of the interface is the development of hierarchical composites based on growth of carbon nanotubes (CNT) on the carbon fibre (CF). The challenge is that during the chemical vapour deposition (CVD) growth of CNTs, surface defects are induced in the CF by diffusion and an etching effect of the Fe catalyst, which alters the tensile properties of the CF. Our approach utilises an Al_2O_3 diffusion barrier layer on the CF surface obtained by atomic layer (ALD). In our present work we deliver the observation of the CF with and without a protective alumina film grafted with CNTs utilising ptychographic X-ray computed tomography (PXCT), which provides 50 nm - resolved 3D electron density maps of the CFs. We present and discuss a data analysis methodology for iron nanoparticle detection in the electron density maps.

1. Introduction

Carbon fibre reinforced polymer (CFRP) composites exhibit excellent tensile properties in the fibre direction, easily overcoming traditional metal solutions in terms of strength- and stiffness-to-mass ratio. Nevertheless, the failure of a CFRP is typically governed by compressive failure in the fibre direction or by insufficient transverse strength. Therefore, there is a high interest to enhance the properties of the fibre-matrix interface. A novel approach is the development of multiscale composites based on growth of nanoscale carbon nanotubes (CNT) at the surface of a microscale carbon fibre (CF) prior to impregnation with polymer [1]. In the direct chemical vapor deposition (CVD) growth conditions of CNTs iron nanoparticles are typically used as a growth catalyst. The major challenge of growth of CNTs on CFs is that the iron tends to induce surface defects of the fibre during growth. These defects strongly diminish the tensile strength of a CF, as tensile failure often originates at a surface defect [2]. If the multiscale composites are to supersede classical CFRP, the tensile properties must be retained, which has been recently approached in ways such as by the choice of an alternative catalyst system [3], [4], alternative CVD reaction mechanisms for CNT growth [4] or utilising a protective layer on the CF surface [5]. The latter was the subject of our study.

The diffusion of iron particles into CF at CVD processing temperatures is not well understood yet. In our present work we deliver the direct observation of the CF with and without a protective ultrathin alumina film utilising ptychographic X-ray computed tomography (PXCT) [6-8] with a high-

Excerpt from ISBN 978-3-00-053387-7

resolution instrument [7]. In the measurement one obtains a 3D electron density map of entire CF cross sections at a resolution of about 50 nm.

2. Experimental

The CF used in the experiments was an unsized type of AS4 produced by Hexcel, USA, that has undergone an oxidative treatment. The CFs have further been coated with thin protective alumina films using atomic layer deposition (ALD). Iron catalyst particles have been deposited on such prepared CFs as well as on neat CFs as a control sample with an electron beam physical vapor deposition (EBPVD) method. Afterwards, the CNTs were grown using a CVD technique based on thermal decomposition of hydrocarbon.

2.1. ALD of Al_2O_3

Atomic layer deposition is a thin film fabrication technique that allows for extremely uniform coating of samples of virtually any geometric complexity while guaranteeing atomic-precision control in layer thickness. This feature of the method makes it ideal for coating of a CF with a barrier layer. The material for the film is chosen to be alumina as it is a popular support for efficient CNT growth [9]. Prior to ALD coating, the samples have undergone ultraviolet / ozone treatment for 10 minutes. The process has been carried out using an ALD system Savannah 100 (Cambridge NanoTech, UK). The precursors for alumina ALD were trimethyl aluminum (TMA) and deionised water. The growth has been carried out at temperature of 225°C. In our previous study the growth rate of the Al_2O_3 film has been calibrated by means of ellipsometry of a silicon wafer placed alongside the CF during the ALD process [5]. In the present study we are investigating oxide film thickness of 11 nm believed to be a sufficient iron diffusion barrier according to our previous study [5].

2.2. EBPVD of the iron catalyst

The Fe catalyst thin film has been delivered onto the surface of fibres using EBPVD. The method relies on physical vaporisation of metal from a target by an accelerated electron beam in vacuum. The vaporized metal gets deposited on the surface of a sample in the reactor. The reactor chamber was held at room temperature and the inside pressure was 1.2×10^{-5} mbar during processing. The deposition rate measured by a quartz balance was set to 0.5 $Å s^{-1}$ by adjusting the electron acceleration voltage prior to opening the shutter. The deposition was stopped at 50 nm film thickness by closing the shutter. To partially overcome the shadowing effect of the technique, the fibres were coated from two opposite sides in separate processes.

2.3. CVD growth of carbon nanotubes on carbon fibre

The CNTs were grown on the samples in a custom atmospheric pressure CVD reactor. The processing parameters were kept constant in a quartz tube oven of 136 mm diameter. The process time was 15 minutes at a temperature of 750°C. The mixture of gases introduced into the reaction chamber was $1\,l\,min^{-1}$ H_2 with $1\,l\,min^{-1}$ ethylene. In this processing step the sputtered iron film is reduced by hydrogen and forms metallic nanoparticles, so the CNT growth can be initiated and continued. The typical catalyst particle diameters are within the range of 20 to 40 nm. The density of particles was estimated as 625 particles per μm^2, as measured by scanning electron microscopy, see Fig. 1.

2.4. Ptychographic X-ray computed tomography for single fibre imaging

The fibre imaging has been conducted at the coherent small angle X-ray scattering (cSAXS) beamline at the Swiss Light Source at the Paul Scherrer Institute, Villigen, Switzerland, using an instrument with high-accuracy positioning between the sample and the illumination while allowing a rotational

Excerpt from ISBN 978-3-00-053387-7

degree of freedom for tomography [7]. We used 7.00 keV photons focused by a Fresnel zone plate (FZP) of 150 µm diameter and 60 nm outermost zone with made of Au [10], with a focal length of 50.82 mm at this energy. The flux provided by the FZP was about 6.4×10^8 photons/s. The sample was placed 1 mm downstream the focus, such that the size of the illumination onto the sample was about 3 µm. Ptychographic scans were performed in a plane perpendicular to the incoming beam at different positions following the pattern of a Fermat spiral [11] with a field of view of 18×10 µm^2 (horizontal × vertical) and with an average distance between points of 0.8 µm. At each scanning position, coherent diffraction patterns with an acquisition time of 0.1 s were recorded with a Pilatus 2M detector with 172 µm pixel size [12] placed 7.355 m downstream the sample. We estimate an incident flux density of 1.2×10^8 photons µm^{-2} for each ptychographic scan. Ptychographic scans were repeated at 375 different angular positions of the specimen with respect to the incoming X-ray beam, covering a total angular range from 0 to 180 degrees with equal angular steps. In order to record data at inactive areas of the detector due to the gaps between detector modules, the position of the detector was changed in the two directions perpendicular to the beam at consecutive angular steps. The total dose deposited on the specimen during a tomographic scan was estimated as described in Ref. [13] to be about 5.1×10^7 Gy, taking into account the mass density of 1.66 g cm^{-3} measured in the CF. Ptychographic reconstructions were performed using the difference map algorithm [14] followed by a maximum likelihood optimization as a refinement step [15]. Each pair of scans recorded at different positions of the detector were combined in the same reconstruction [16], allowing two different images to be reconstructed for different angles while sharing the same illumination, as introduced in Ref. [7]. For ptychographic reconstructions an area of 600×600 pixels of the detector was used, obtaining images with a pixel size of 12.62 nm. The reconstructed images are a measurement of the complex-valued transmissivity of the sample at different incidence angles. The phase images were further processed to correct zero- and first-order terms, which are intrinsic degrees of freedom in ptychographic reconstructions, and registered before tomographic reconstruction as described in Ref. [17]. The resolution of the final 3D images was estimated to be about 50 nm. For determining the resolution we compared the Fourier ring correlation of two subtomograms, each of them computed with half of the angular projections, with the half-bit threshold, as described in Ref. [18]. In this work we focus on two measurements of CFs with and without a protective alumina film grafted with CNTs and on the development of a methodology for data analysis for the investigation of iron nanoparticles embedded in CFs in the CVD growth process.

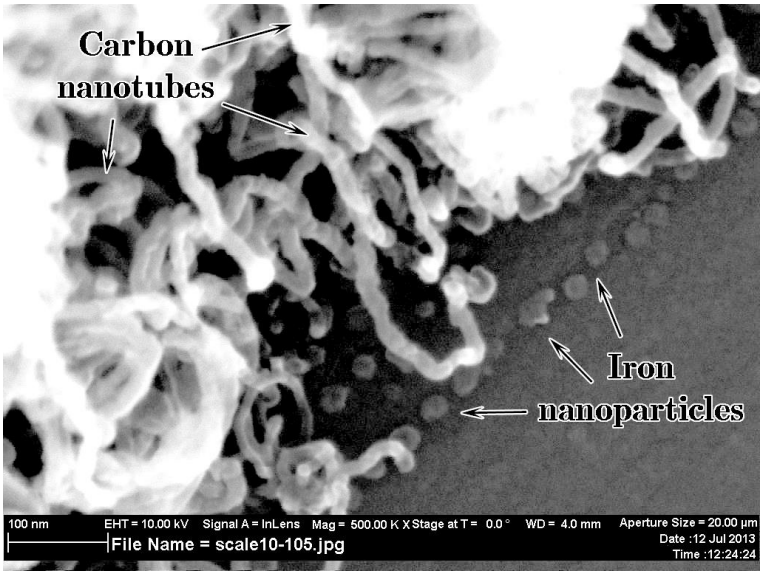

Figure 1. SEM image of iron nanoparticles and grown CNTs on the surface of a CF.

Excerpt from ISBN 978-3-00-053387-7

3. Results and discussion

3.1. Set of examined samples

Using the methods described in 2.1-2.3, two groups of samples have been prepared: control samples of CF without the protective alumina film and CF with an ultrathin 11 nm alumina. All the samples were coated with an Fe catalyst film of nominal thickness 50 nm and CNTs were grown on each one using CVD.

3.2. Assessment of the electron density of the materials present in the samples

PXCT provides 3D maps of the electron density distribution within each CF. The electron density of a material can be calculated as

$$\varrho_e = \frac{\Delta N_e}{\Delta V} = \frac{\varrho N_\mathrm{A}}{\mu} \sum_i N_i Z_i \tag{1}$$

where ϱ_e is the electron density, ϱ is the mass density of the material, N_A is the Avogadro number, μ is the molar mass of a stoichiometric unit of the material, i is the index of an element present in the material, N_i is the number of atoms of the i-th element in a stoichiometric unit of the material and Z_i is the atomic number of the element. In our case there are three materials to consider: the bulk of carbon fibre, α-iron of nanoparticles being the phase of iron at room temperature and alumina of the film. In our analysis we do not consider the CNTs. The parameters are summarized in Table 1.

Table 1. Properties of the materials considered in our analysis. The stoichiometry of carbon fibre is taken fractional as the CF is predominantly a mixture of C and N. Electron density calculated according to (Eq. 1).

Material	Density	Stoichiometry	Molar mass	Atomic numbers	Electron density
Alumina	3.0 g cm^{-3} [19]	Al_2O_3	101.96 g mol^{-1}	$_{13}$Al, $_{8}$O	0.89 Å^{-3}
CF	1.79 g cm^{-3}[20]	$C_{0.94}N_{0.06}$ [20]	12.13 g mol^{-1}	$_{6}$C, $_{7}$N	0.54 Å^{-3}
α-Iron	7.84 g cm^{-3}	Fe	55.85 g mol^{-1}	$_{26}$Fe	2.21 Å^{-3}

The electron density values in the table show that the iron nanoparticles, having more than four times larger electron density than the CF, should appear as voxel groups of elevated electron density. On the other hand, thin alumina film has not more than twice the electron density of the CF and it is also thinner than the expected resolution of the PXCT, therefore it might be not clearly visible in the electron density map. Considering the fact that the 11 nm film of alumina is expected to prevent the iron infusion, it is explicitly observed in the maps that the high-density voxels are always on the surface of a CF and never underneath it, see Figure 2 b. The control samples without protection exhibit presence of iron below the surface, see Figure 2 a. Here we show only two slices, but this observation extends to all slices over the 10 μm field of view of the measurements.

3.3. The automated fitting of CF position in the electron density maps

The 3D electron density maps of each sample can be understood as stacks of 2D slices perpendicular to the fibre. To analyse the data spatially, we fit the CF surface to a cylinder with an automatic reliable algorithm. This is performed in the following way:

- The cylinder has an elliptical cross section for the sake of generality.
- For each slice the largest ellipse which fits inside the CF is sought. The size parameter of the ellipse is defined as the sum of squares of its axes a and b. The criterion for the ellipse

Excerpt from ISBN 978-3-00-053387-7

to be inside CF is that all the voxels of the ellipse edge must represent electron density not lower than $0.4\ \text{Å}^{-3}$. The value was chosen arbitrarily as smaller than the electron density of the CF giving the best fitting results and it can be adjusted to the needs of a specific case. As a result, for each slice we have a set of parameters: position of the center or the ellipse $\vec{r}_0$, its axes a and b and a rotation angle of the ellipse around its center ϑ.

- The lengths of axes and the ellipse rotation angle are taken as mean values of a, b, and ϑ from all 2D slices, whereas the center position is calibrated using a linear fit of $\vec{r}_0$ as a function of the z coordinate of each slice.

If the CF axis significantly deviated from the perpendicular to the map axis z, it would be necessary to take into account this fact in the analysis. However, in the analysis it appeared that the angle never deviated from 90° by more than 1°, which is why it was convenient to assume that the slices are perpendicular to the fibre axis, which introduced a relative systematic error of x, y coordinates within each slice of $(1/\cos 1°) - 1 \approx 2 \times 10^{-4}$. The spatial error might be assessed taking the expected radius of the CF 3.5 µm and multiplying it by 2×10^{-4}, giving 0.7 nm, which is much smaller than the spatial resolution of about 50 nm, therefore it can be neglected and the assumption that the fibre axis is perpendicular to the planes of slices is justified.

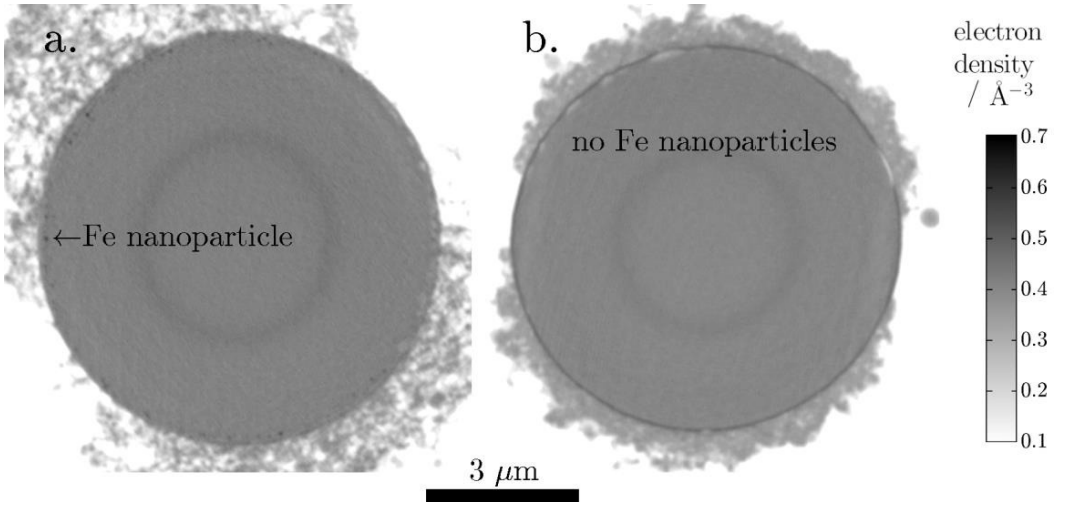

Figure 2. Representative slices of CFs electron density maps; a. An unprotected CF exhibits presence of iron nanoparticles below the CF surface; b. A CF with an 11 nm alumina film shows no iron nanoparticles below surface.

4. Electron density distributions

To reveal the presence of iron within the carbon fibre without the Al_2O_3 protection film, it is necessary to analyse the electron density distributions. Two histograms of the electron density values were prepared in two regions of the CF: in a region where iron nanoparticles are observed close to the CF surface – within a 30 nm thick surface below the CF surface that crosses multiple iron nanoparticles, and in the other region where they are absent - 30 nm thick surface that does not cross any iron nanoparticle, see Figure 3. Each histogram accounted around 2 mln voxels.

In the histogram of the iron-rich region we cannot explicitly resolve any high electron density peak that could have been attributed to the presence of iron nanoparticles. It might be due to the fact that the size of the nanoparticles is below the resolution of the method. However, in the histogram one can observe a long shoulder reaching large electron densities due to partial volume effects. Such an effect was not observed for the protected CF and for the unprotected CF in regions where nanoparticles were not observed, therefore we reason that it is a good indicator of abundance of iron nanoparticles.

Excerpt from ISBN 978-3-00-053387-7

A Gaussian fit to the curve for negligible iron content gives the mean electron density of CF $x_0 = (50.16 \pm 0.16) \times 10^{-2}$ Å^{-3} which is slightly lower than the expected value 0.54 Å^{-3} from Table 1 and would correspond to a mass density of $1.66\,\mathrm{g\,cm^{-3}}$. The standard deviation of the Gaussian curve is $\mathrm{rms} = (25.82 \pm 0.36) \times 10^{-3}$Å^{-3}, corresponding to the rms of the measurement noise. Moreover, in the graph it can be seen that when iron is absent, the electron density should almost never go higher than 0.62 Å^{-3}. Therefore this value can be taken as a threshold T for detection of iron in the given voxel, both for 11 nm Al_2O_3-protected and unprotected carbon fibre.

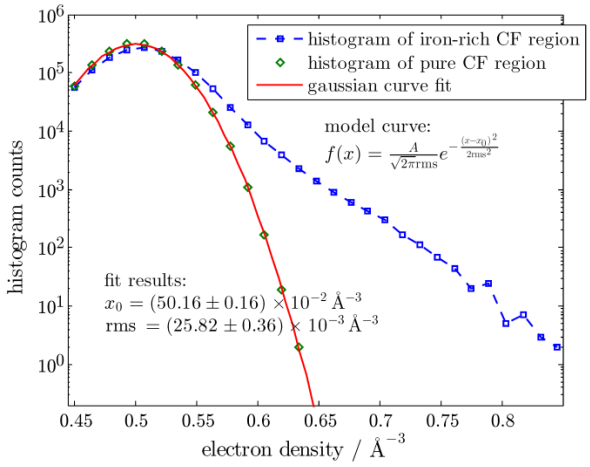

Figure 3. Histograms of the electron density values within two different regions of the CF without alumina barrier layer: region where Fe nanoparticles are present (blue squares) and one where they are absent (green diamonds) with a Gaussian curve fit (red line).

It can be argued that a thin alumina film might be erroneously detected as iron. To simulate the detected electron density in the case that an alumina film is present, we can consider the physical appearance of the film as a combination of step functions

$$\varrho(x) = \varrho_{Al_2O_3} h(x+\delta) + (\varrho_{CF} - \varrho_{Al_2O_3}) h(x), \tag{2}$$

where x is the spatial coordinate corresponding to the depth into the CF, δ is the thickness of the Al_2O_3 film, $\varrho(x)$ is the actual electron density at a given coordinate, ϱ_{CF} is the carbon fibre electron density, $\varrho_{Al_2O_3}$ is the electron density of the alumina, $h(x)$ is the unit step function. We assume that the resolution effect exhibits a Gaussian behavior. In such a case, two features are resolvable when the distance between them is larger than two standard deviations of a Gaussian kernel. Therefore, as an estimate of the standard deviation of the kernel we take half of the resolution value, $\sigma = 25$ nm. We can estimate the measured electron density as a convolution of $\varrho(x)$ with a Gaussian.

$$(\varrho * G)(x) = \varrho_{Al_2O_3} \frac{1 + \mathrm{erf}\left(\frac{x+\delta}{\sqrt{2}\sigma}\right)}{2} + (\varrho_{CF} - \varrho_{Al_2O_3}) \frac{1 + \mathrm{erf}\left(\frac{x}{\sqrt{2}\sigma}\right)}{2}, \tag{3}$$

where $G(x)$ is a Gaussian distribution with mean value 0 and standard deviation σ

$$G(x) = \frac{1}{\sqrt{2\pi}\sigma} e^{-\frac{x^2}{2\sigma^2}}. \tag{4}$$

The functions (Eq. 2,3) are shown in Figure 4a. The Gaussian noise with the $\mathrm{rms} = 0.025$ Å^{-3} was added to the function (Eq. 3). In the graph it can be noticed that despite the sharp jump in the electron density in the alumina region, the voxels of alumina are very unlikely to be erroneously detected as iron given the threshold of $T = 0.62$ Å^{-3}. Additionally it can be considered how large iron nanoparticles will be detected using the defined threshold. For this purpose we have performed numerical calculations simulating the detected peak value with respect to the size of an iron nanoparticle embedded

Excerpt from ISBN 978-3-00-053387-7

in a matrix of carbon fibre body. Initially, we defined a 3D electron density map of a spherical iron particle of a given diameter embedded in a body of a CF. The map has been convolved with a three-dimensional Gaussian distribution with the same σ as before. From such an electron density map its peak value has been extracted. Assuming that the electron density noise exhibits a Gaussian behaviour, the probability of detection of the nanoparticle can be estimated as

$$p(d) = \frac{1}{2}\left(1 + \mathrm{erf}\left(\frac{\varrho_{\max}(d) - T}{\sqrt{2}\mathrm{rms}}\right)\right), \tag{5}$$

where p is the detection probability, d is a nanoparticle diameter, $\varrho_{\max}$ is the peak value of a given simulated electron density map for a given d, T is the iron detection threshold. The curve resulting from the presented considerations is illustrated in Figure 4b. From the curve we can reason that almost all nanoparticles of diameter greater than 38 nm will be detected using the defined threshold. Nanoparticles of diameter 33 nm already cross the 50% detection probability.

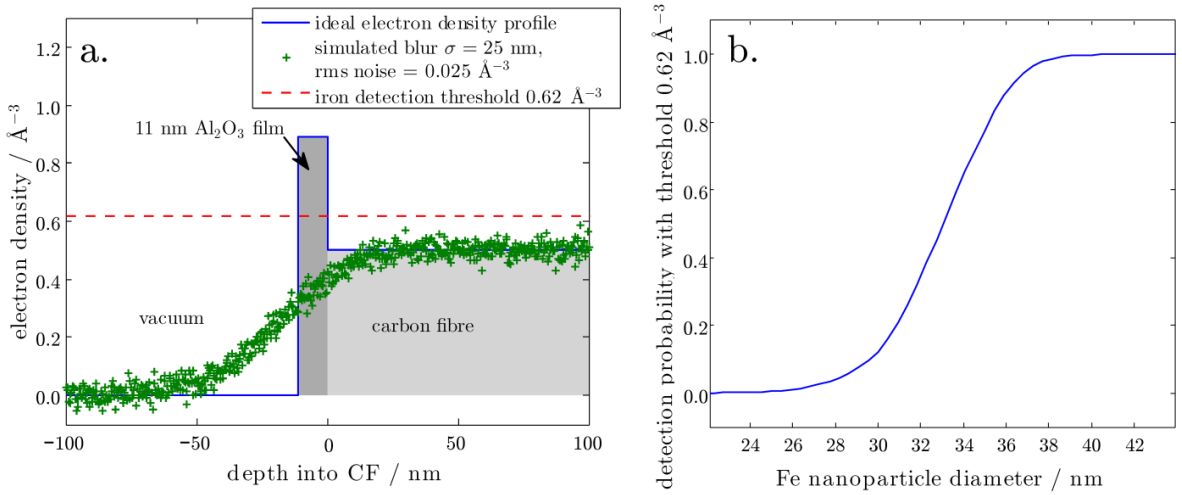

Figure 4. a. Simulated electron density profile of CF coated with 11 nm Al_2O_3 film – explicit sharp-edge curve (Eq. 2) and simulated blurred detection curve with noise assuming spatial resolution of 50 nm and noise of 0.025 $Å^{-3}$ rms (Eq. (3)). The $T = 0.62$ $Å^{-3}$ threshold is shown;
b. The detection probability of iron nanoparticle surrounded by the bulk of a carbon fibre.

5. Summary and conclusion

In this work we present the direct observation of carbon fibres with and without a protective ultrathin alumina film grafted with CNTs using ptychographic X-ray computed tomography. We have developed a number of analytical tools to analyse the 3D density maps of CFs in order to detect the presence of Fe nanoparticles that are not spatially resolved in the tomograms. First of all, we have used histograms of the electron density at different regions inside fibre to determine the detection threshold of iron nanoparticles. We have proven semi-analytically that using this threshold an ultrathin alumina film is unlikely to be erroneously detected as an iron nanoparticle. We have also estimated numerically that with the defined threshold the detection probability of nanoparticles of 33 nm diameter is approximately 50% whereas for nanoparticles of diameter greater than 38 nm it is almost 100%. The results obtained are very significant for the further understanding and control of the iron infiltration phenomenon into a CF during CVD growth of CNTs for hierarchical composites.

Acknowledgements

We thank Andreas Menzel for his feedback on the manuscript.

Excerpt from ISBN 978-3-00-053387-7

References

[1] H. Qian, E. S. Greenhalgh, M. S. P. Shaffer, and A. Bismarck. Carbon nanotube-based hierarchical composites: a review, *J. Mater. Chem.*, vol. 20, no. 23, p. 4751, 2010.
[2] J. W. Johnson and D. J. Thorne. Effect of internal polymer flaws on strength of carbon fibres prepared from an acrylic precursor, *Carbon*, vol. 7, no. 6, pp. 659–661, Dec. 1969.
[3] R. Cartwright, S. Esconjauregui, D. Hardeman, S. Bhardwaj, R. Weatherup, Y. Guo, L. D'Arsié, B. Bayer, P. Kidambi, S. Hofmann, E. Wright, J. Clarke, D. Oakes, C. Cepek, and J. Robertson. Low temperature growth of carbon nanotubes on tetrahedral amorphous carbon using Fe–Cu catalyst, *Carbon*, vol. 81, pp. 639–649, Jan. 2015.
[4] N. De Greef, L. Zhang, A. Magrez, L. Forró, J.-P. Locquet, I. Verpoest, and J. W. Seo. Direct growth of carbon nanotubes on carbon fibers: Effect of the CVD parameters on the degradation of mechanical properties of carbon fibers, *Diam. Relat. Mater.*, vol. 51, pp. 39–48, Jan. 2015.
[5] S. Vogel, C. Dransfeld, C. Schönenberger, and J. Gobrecht. Protective effect of thin alumina layer on carbon fibre to preserve tensile strength during CNT growth by CVD, *Proceedings of the 16th European Conference on Composite Materials ECCM16, Seville, Spain,* June 22-26 2014.
[6] A. Diaz, M. Guizar-Sicairos, A. Poeppel, A. Menzel, and O. Bunk. 'Characterization of carbon fibers using X-ray phase nanotomography', *Carbon*, vol. 67, pp. 98–103, Feb. 2014.
[7] M. Holler, A. Diaz, M. Guizar-Sicairos, P. Karvinen, E. Färm, E. Härkönen, M. Ritala, A. Menzel, J. Raabe, and O. Bunk. X-ray ptychographic computed tomography at 16 nm isotropic 3D resolution, *Sci. Rep.*, vol. 4, Jan. 2014.
[8] M. Dierolf, A. Menzel, P. Thibault, P. Schneider, C. M. Kewish, R. Wepf, O. Bunk, and F. Pfeiffer. Ptychographic X-ray computed tomography at the nanoscale, *Nature*, vol. 467, no. 7314, pp. 436–439, Sep. 2010.
[9] M. Kumar and Y. Ando. Chemical Vapor Deposition of Carbon Nanotubes: A Review on Growth Mechanism and Mass Production, *J. Nanosci. Nanotechnol.*, vol. 10, no. 6, pp. 3739–3758, Jun. 2010.
[10] S. Gorelick, J. Vila-Comamala, V. A. Guzenko, R. Barrett, M. Salomé, and C. David. High-efficiency Fresnel zone plates for hard X-rays by 100 keV e-beam lithography and electroplating, *J. Synchrotron Radiat.*, vol. 18, no. 3, pp. 442–446, May 2011.
[11] X. Huang, H. Yan, R. Harder, Y. Hwu, I. K. Robinson, and Y. S. Chu. Optimization of overlap uniformness for ptychography, *Opt. Express*, vol. 22, no. 10, p. 12634, May 2014.
[12] B. Henrich, A. Bergamaschi, C. Broennimann, R. Dinapoli, E. F. Eikenberry, I. Johnson, M. Kobas, P. Kraft, A. Mozzanica, and B. Schmitt. PILATUS: A single photon counting pixel detector for X-ray applications, *Nucl. Instrum. Methods Phys. Res. Sect. Accel. Spectrometers Detect. Assoc. Equip.*, vol. 607, no. 1, pp. 247–249, Aug. 2009.
[13] M. R. Howells, T. Beetz, H. N. Chapman, C. Cui, J. M. Holton, C. J. Jacobsen, J. Kirz, E. Lima, S. Marchesini, H. Miao, D. Sayre, D. A. Shapiro, J. C. H. Spence, and D. Starodub. An assessment of the resolution limitation due to radiation-damage in X-ray diffraction microscopy, *J. Electron Spectrosc. Relat. Phenom.*, vol. 170, no. 1–3, pp. 4–12, Mar. 2009.
[14] P. Thibault, M. Dierolf, A. Menzel, O. Bunk, C. David, and F. Pfeiffer. High-Resolution Scanning X-ray Diffraction Microscopy, *Science*, vol. 321, no. 5887, pp. 379–382, Jul. 2008.
[15] P. Thibault and M. Guizar-Sicairos. Maximum-likelihood refinement for coherent diffractive imaging, *New J. Phys.*, vol. 14, no. 6, p. 63004, Jun. 2012.
[16] M. Dierolf, Ptychographic X-ray Microscopy and Tomography, PhD Thesis, Technical University Munich, Germany, 2015.
[17] M. Guizar-Sicairos, A. Diaz, M. Holler, M. S. Lucas, A. Menzel, R. A. Wepf, and O. Bunk. Phase tomography from x-ray coherent diffractive imaging projections, *Opt. Express*, vol. 19, no. 22, p. 21345, Oct. 2011.
[18] M. van Heel and M. Schatz. Fourier shell correlation threshold criteria, *J. Struct. Biol.*, vol. 151, no. 3, pp. 250–262, Sep. 2005.
[19] S. M. George. Atomic Layer Deposition: An Overview, *Chem. Rev.*, vol. 110, no. 1, pp. 111–131, Jan. 2010.
[20] 'www.hexcel.com/Resources/DataSheets/Carbon-Fiber-Data-Sheets/AS4.pdf'.

Excerpt from ISBN 978-3-00-053387-7